PAPER

Check for updates

Enhancing visible-light photocatalytic performance of Au/TiO$_2$ catalysts through light reflection-promoted optical absorption with oriented anatase mesocrystals†

Jingling Yang,[ab] Shiman He,[b] Hongwei Liu,[c] Esa Jaatinen,[d] Eric Waclawik,[d] Jiamin Quan,[e] Sarina Sarina, [d] Chun He, [f] Senchuan Huang,[b] Huaiyong Zhu *[d] and Mingmei Wu *[b]

Au nanoparticles (NPs) attached to various TiO$_2$ supports are widely studied as plasmonic catalysts for driving chemical reactions under visible light irradiation. However, plasmonic catalysis still suffers from unsatisfactory efficiencies due to limited light-harvesting abilities. Here we reported a new tactic to enhance the light-harvesting ability of plasmonic Au NPs by utilizing a light reflection-promoted model – a vertically <001> oriented anatase mesocrystal (*meso*-TiO$_2$) rooted on Ti foil as the support, and thus achieving efficient photocatalytic sulfur-containing volatile organic compound elimination and hydrogen evolution from water. Experimental evidence and theoretical simulations confirm that the Au NPs in this architecture more effectively harvest visible light because of the simultaneous absorption of both the incident and the back-reflected photons from the *meso*-TiO$_2$/Ti foil surface, where Ti foil serves as the reflective substrate. The enhanced light absorption of Au NPs in this light reflection-promoted model excited strong localized surface plasmon resonance to yield more reactive species that drive the redox reactions. This research could inspire a new paradigm to improve the photocatalytic performance of plasmonic metals by utilizing the light reflection model.

1. Introduction

Plasmonic catalysts of Au nanoparticles (NPs) dispersed on TiO$_2$ supports have been studied for a wide range of applications in chemical synthesis, energy innovation and pollution remediation.[1–8] The Au NPs can effectively absorb visible light due to the localized surface plasmon resonance (LSPR) effect, which can promote the migration of hot electrons from the Au NPs to the TiO$_2$ support.[9,10] Both the hot electrons transferred to the support and positively charged holes remaining on the Au NPs can induce chemical reactions. Plasmonic catalysts operate in a manner that is fundamentally different from conventional semiconductor catalysts in the nature of their light harvesting, charge generation and migration,[11] energy transfer,[12] and interaction between the catalyst and reactants.[13] Significant effort has been dedicated to improving the performance of the plasmonic catalysts under visible light irradiation.[7]

The quantum yield of light absorption is a primary factor in determining photocatalytic performance.[9] Even though the absorption of visible light by a single Au NP a few nanometers in size can be significant, a large fraction of the total incident light is transmitted when light is directed onto a surface that has been coated with a film of the plasmonic metal Au, and a significant fraction is transmitted to the underlying substrate if the effective gold thickness is thin.[6,14] For Au NPs with diameters <10 nm the light energy transmitted is considerable. Unlike Au NPs, TiO$_2$ absorbs only a negligible amount of visible light, particularly when in the form of a thin TiO$_2$ film. The crystal properties of TiO$_2$, such as the crystal size, orientation, defects, and inter-crystal voids, all influence its light reflection and scattering and, therefore, the level of photon loss. It follows then that the light absorption by the Au NPs on a TiO$_2$ support will be considerably affected.[15–19] If the catalyst is designed to maximize light reflection and their absorption by using Au NPs, the efficiency of the catalyst should be substantially improved.

[a]Guangdong Key Laboratory of Environmental Pollution and Health, School of Environment, Jinan University, Guangzhou 510632, P. R. China

[b]School of Chemical Engineering and Technology, School of Chemistry, Sun Yat-Sen University, Guangzhou 510275, P. R. China

[c]Australian Centre for Microscopy & Microanalysis, The University of Sydney, Sydney, NSW 2006, Australia

[d]School of Chemistry, Physics and Mechanical Engineering, Queensland University of Technology, Brisbane, QLD4001, Australia

[e]The Key Laboratory of Optoelectronic Technology & System, Education Ministry of China, Chongqing University, 400044, China

[f]School of Environmental Science and Engineering, Sun Yat-Sen University, Guangzhou, 510275, P. R. China

† Electronic supplementary information (ESI) available. See DOI: https://doi.org/10.1039/d2ta09982a

This journal is © The Royal Society of Chemistry 2023

J. Mater. Chem. A, 2023, 11, 4751–4757 | **4751**

TiO$_2$ crystals can be essentially transparent to visible light if TiO$_2$ is aligned, which forms an essentially crystalline structure to minimize light scatter. As illustrated in Scheme 1, we envisioned that if the light transmitted through the overlying layer of Au NPs and underlying nanostructured TiO$_2$ could be reflected from the Ti foil back to the metal NPs, the total amount of light being absorbed by these Au NPs would increase,[15] which could be expected to improve the yield of photocatalytic reaction for this composite system.

To verify the above assumption, in this present study, Au NPs were attached to the <001> oriented TiO$_2$ mesocrystals that were supported by a piece of reflective Ti foil to reflect the light transmitted through the overlying nanostructure (see Scheme 1a). Mesocrystals are highly ordered superstructures with a high degree of crystallinity and oriented subunit alignment.[20] For comparison, less transparent films were studied that consisted of aggregated small anatase polycrystals arranged without a preferred orientation (see Scheme 1b). The visible light photocatalytic performance of the three catalysts was evaluated for two model reactions, methanethiol (CH$_3$SH) removal by catalytic oxidation and H$_2$ evolution by reducing water, which are two redox reactions.

CH$_3$SH is a representative sulfur-containing volatile organic compound (S-VOC) with significant toxicity, and photocatalysis is an efficient way for CH$_3$SH elimination,[21,22] while hydrogen production from water is a cost-effective approach to promote the development of future hydrogen economies.[23] This work using a TiO$_2$ mesocrystal to tune the optical absorption of Au NPs and their performance for catalytic redox reaction highlights the support-effect induced efficient utilization of reflected light, and hence, understanding the effect of light reflection-promoted optical absorption would provide guidelines for designing efficient photocatalysts.

2. Experimental section

2.1 Preparation of a Au/TiO$_2$ film

The fabrication process of the anatase-type TiO$_2$ film on a piece of Ti foil with a size of 1×1 cm^2 was performed by the
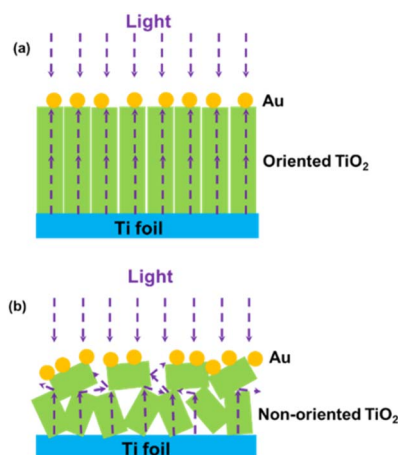
acid vapor oxidation (AVO) reaction at 140 °C in an autoclave for 12 or 60 h, respectively.[25] The details are shown in the ESI.† The as-synthesized anatase-type TiO$_2$ mesocrystal film with a fabrication time of 12 h was denoted as *meso*-TiO$_2$, and the TiO$_2$ polycrystal films with a fabrication time of 60 h were denoted as *p*-TiO$_2$. A Degussa P25 (TiO$_2$) film was prepared by slowly dipping the titanium foil into an ethanol solution containing TiO$_2$ Degussa P25 (10 g L^{-1}) for 5 min and then taking it out; the same procedure was repeated six times, and it was then dried at 100 °C for 12 h. Subsequently, Au NPs were deposited onto these TiO$_2$ films by the UV-assisted photocatalytic reduction method: the TiO$_2$ film was soaked in 5.0 mL of aqueous HAuCl$_4$ (5 mmol L^{-1}), irradiated with UV light for 15 min to reduce the Au^{3+} adsorbed by TiO$_2$ to Au NPs, then rinsed with distilled water to remove the remaining substances on the film surface and dried in a vacuum oven at room temperature for 12 h.

2.2 Characterization

X-Ray diffraction (XRD) patterns were recorded on a Bruker D8 Advance with Cu Kα radiation (40 kV, 40 mA). The microstructural properties were characterized using electron microscopy. Scanning electron microscopy (SEM) images were obtained on an FEI Quanta 400F electron microscope. Transmission electron microscopy (TEM) images, high-resolution TEM (HRTEM) images, and element mapping results were taken on an FEI Tecnai G2 F30 electron microscope operated at 300 kV, and JEOL JEM-2100F electron microscope operated at 200 kV. X-ray photoelectron spectroscopy (XPS) spectra were measured using an X-ray photoelectron spectrometer (ESCA-LAB 250). A UV-2450 spectrophotometer was used to obtain ultraviolet-visible (UV-vis) diffuse reflectance spectra of these products using BaSO$_4$ as a reference sample. The fluorescence emission enhancement spectra of the samples were collected on an Edinburgh Instruments FLS920 with a 450 W xenon lamp as the excitation source. The sample films for fluorescence enhancement measurement were prepared in the following manner: one piece of the sample film was slowly dipped into a solution of RhB (10^{-4} mol L^{-1}) for five min and then dried in a vacuum drier at room temperature. The excitation wavelength was 540 nm. The hydroxyl radicals (˙OH) and superoxide radicals (˙O$_2^-$) were detected using a Bruker A300-10-12 electron spin resonance spectrometer (ESR, Bruker, Germany) with a 150 W short arc xenon lamp as the irradiation light source and 5,5-dimethyl-1-pyrroline N-oxide (DMPO) as a spin trap agent. The details are shown in the ESI.† The loading amount of Au on the samples was measured using an inductively coupled plasma-mass spectrometer (ICP-MS) (Agilent 7700e). The transient photocurrents were measured on an electrochemical workstation (Metrohm Autolab PGSTAT302N, Herisau, Switzerland), where the samples, Ag/AgCl, and Pt wire served as working, reference, and counter electrodes, respectively. The photocurrent was measured at an applied potential of 0.4 V (*vs.* Ag/AgCl), and the electrolyte was 0.5 mol L^{-1} of Na$_2$SO$_4$ aqueous solution. The illumination source was

Scheme 1 Illustration of light reflection behavior of oriented anatase TiO$_2$ (a) and non-oriented TiO$_2$ (b) under light irradiation.

4752 | *J. Mater. Chem. A*, 2023, **11**, 4751–4757

This journal is © The Royal Society of Chemistry 2023

a 300 W Xe lamp (Perfect light PLS-SXE300CUV, Beijing, China) with a visible light filter ($\lambda \geq 430$ nm).

2.3 Photocatalytic removal of CH₃SH

The photocatalytic removal of CH_3SH was conducted by fixing the sample films in the middle of a cylindrical quartz cell equipped with a CH_3SH detector (DM-400IS, Detcon) in the range of 0–100 ppm per v ($\pm 2\%$), with a detection limit of 0–100 ppm per v and reproducibility of 2%. Subsequently, the CH_3SH flow continuously passed through a catalyst-filled reactor with a constant inflow of 100 mL min^{-1}. Air was employed to dilute CH_3SH at an influent concentration of 50 ppm. The inlet and outlet concentrations of CH_3SH were analyzed by using a CH_3SH detector. A 150 W Xe arc lamp was used as a light source (Beijing Saifan 7ILX150P) with a visible light filter ($\lambda \geq 430$ nm and irradiation power = 10–20 mW cm^{-2}). The light was vertically incident on the samples, and the samples were all immobilized on Ti foil. After adsorption for 1.0 min at room temperature, the light was turned on to reach the adsorption equilibrium. All the tests were carried out under ambient conditions at a temperature of 25 °C.

2.4 Photocatalytic hydrogen evolution

The samples were inserted at the bottom of a cylindrical quartz cell filled with 200 mL of a water/methanol mixture (170/30 vol%) at pH = 6.4. The cell was purged with bubbling N_2 gas for 20 min and sealed with a rubber septum. A 300 W Xe arc lamp was used as a light source with a visible light filter (20CGA-430, Newport Corporation, visible light $\lambda \geq 430$ nm, and

irradiation power = 20 mW cm^{-2}). The light source is vertically incident on the samples, and the samples are all immobilized on Ti foil (Fig. S9†). All the experiments lasted for 8.0 h, and gas samples were withdrawn and analyzed by gas chromatography (GC-7920, Lunan Xinke) to verify H_2 evolution.

3. Results and discussion

3.1 Synthesis, microstructure observations, and optical property analyses

The film fabrication process, where Au NPs were deposited onto <001> oriented anatase-type TiO_2 mesocrystals (*meso*-TiO_2), is schematically illustrated in Fig. 1a. Both <001> oriented *meso*-TiO_2 and non-orientated polycrystalline *p*-TiO_2 rooted at the Ti foil base were fabricated using an acid vapor oxidation (AVO) strategy with Ti foil as tje titanium source under consistent identical reaction conditions but with different duration times. The formation of <001> oriented *meso*-TiO_2 is attributed to a topotactic conversion from the hexagonal $TiOF_2$ intermediate *via* acid vapor oxidation (AVO) (Fig. S1†), and the prolonged oxidation time results in the formation of a non-orientated TiO_2 polycrystal (*p*-TiO_2) as we previously reported.[25] Au NPs were deposited on the top surface of the *meso*-TiO_2 and *p*-TiO_2 substrates *via* a facile photoreduction method.[24] Au NPs were also loaded onto the film of the Degussa P25 polycrystal deposited on Ti foil *via* the same approach.

The X-ray diffraction (XRD) peaks of *meso*-TiO_2, *p*-TiO_2, Au/*meso*-TiO_2 and Au/*p*-TiO_2, as shown in Fig. 1b and S2,† can be indexed to tetragonal anatase-type TiO_2 (JCPDS No. 21-1272). The XRD patterns of *meso*-TiO_2 and Au/*meso*-TiO_2 show sharp (004) diffraction peaks. The calculated crystallographic

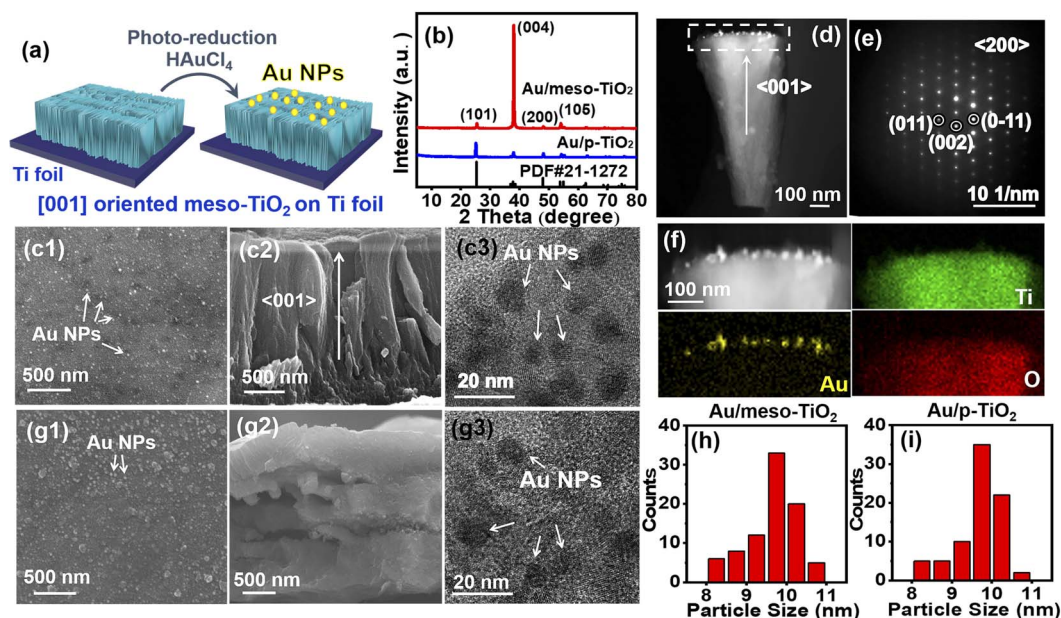**Fig. 1** Preparation and structural characterization. (a) Illustration of the preparation of Au/*meso*-TiO_2. (b) XRD patterns. SEM images with (c1) top-view and (c2) side-view, (c3) high-magnification TEM image of the top-view, (d) cross-sectional STEM image, (e) SAED pattern, and (f) element mappings of Au/*meso*-TiO_2. (g) SEM images and high-magnification TEM images of Au/*p*-TiO_2. The size distributions of Au NPs in (h) Au/*meso*-TiO_2 and (i) Au/*p*-TiO_2.

This journal is © The Royal Society of Chemistry 2023

J. Mater. Chem. A, 2023, **11**, 4751–4757 | **4753**

preferred orientation (CPO) of *meso*-TiO$_2$ along the <001> direction reaches nearly 100%, indicating a strong orientation along the <001> direction with large crystal size and high crystallinity.[25] In contrast, the *p*-TiO$_2$ in Au/*p*-TiO$_2$ has no distinguishable orientation. No obvious peaks from the Au NPs were observed because of the low loading quantity of Au. The scanning electron microscope (SEM) images, transmission electron microscope (TEM) images, and STEM image of Au/*meso*-TiO$_2$ in Fig. 1c and d confirmed that *meso*-TiO$_2$ is assembled by highly oriented subunits that grew vertically on the Ti foil, while the corresponding selected area electron diffraction (SAED) pattern shows the single crystalline nature of *meso*-TiO$_2$ that arranged along the <001> axis (Fig. 1e). The single-crystal-like structure reveals its mesocrystalline nature due to the oriented assembly of nanoflakes where the constituting crystallites are arranged along a shared crystallographic register.[25] Moreover, the top-view SEM image (Fig. 1c1) and the element mapping images (Fig. 1f) reveal that Au NPs are attached to the top surface of the *meso*-TiO$_2$. As a control, dispersed Au NPs are also observed in the *p*-TiO$_2$ and P25 films (Fig. 1g and S3c–f†). However, the anatase-type *p*-TiO$_2$ in Au/*p*-TiO$_2$ and the P25 particles in Au/P25 demonstrate non-oriented polycrystalline properties, with a rough surface structure and voids between the crystals. Au/*meso*-TiO$_2$, Au/*p*-TiO$_2$, and Au/P25 are identified to have an identical thickness of 4–5 μm (Fig. 1c2, g2 and S3e†). The XPS spectrum (Fig. S4†) confirms that the Au NPs in Au/*meso*-TiO$_2$ exist in metallic gold.

The above results collectively confirm the strong orientation, large crystal size and high crystallinity that occurs in the Au/*meso*-TiO$_2$ sample, and Au/*p*-TiO$_2$ and Au/P25 samples have a disordered polycrystalline structure. The size distributions of Au NPs in Fig. 1h, i and S3d† show that the size of Au NPs in Au/

meso-TiO$_2$ is *ca.* 9.7 nm, comparable to the Au NPs in Au/*p*-TiO$_2$ and Au/P25. The specific surface area (S_{BET}) of Au/*meso*-TiO$_2$, Au/*p*-TiO$_2$ and Au/P25 is 18.2, 21.8 and 56.3 m^2 g^{-1} (Fig. S5†), respectively. The surface area of Au/*meso*-TiO$_2$ was slightly lower than that of Au/*p*-TiO$_2$ because there were fewer inter-crystal voids. The quantity of Au in the as-synthesized samples was revealed; the Au content was found to be 2.0 wt% in Au/*meso*-TiO$_2$, identical to the 2.0 wt% in the Au/*p*-TiO$_2$ sample, and similar to the 2.1 wt% in the Au/P25 sample (Fig. S6 and Table S1†). These results collectively confirm the identical size and morphology of Au NPs in these samples. Based on the comparable size distributions and amounts of Au NPs, a comparative study of the influence of the TiO$_2$ support on the light-capturing properties of Au could be made.

Visible light transmission through the Au/TiO$_2$ samples was calculated based on the Beer–Lambert law. The calculation model is shown in Fig. 2a and S7.† The scheme in Fig. 2a shows how the Au NPs absorb the incident light and back reflection from the TiO$_2$-titanium foil. When visible light illuminates the Au NP layer, 80% of the incident light is transmitted through Au NPs and TiO$_2$ to the highly reflective titanium foil. Then, the transmitted light is reflected by the foil back to Au/TiO$_2$. The Au NPs absorb the reflected light with a small fraction of unharvested light (equal to 24% of the incident light). The absorption of the reflected light significantly increases the light-harvesting ability of Au NPs. The calculated specific proportion of light transmission through the substrate depends on the gold thickness and the value of the scatter level of TiO$_2$ (Fig. 2b and c). It is known from Mie scattering theory that for Au NPs less than 20 nm in diameter, the smaller the Au NP diameter, the greater the fraction of incident light that is transmitted to the TiO$_2$ support. For Au NPs which have diameters of 9.7 nm bound to
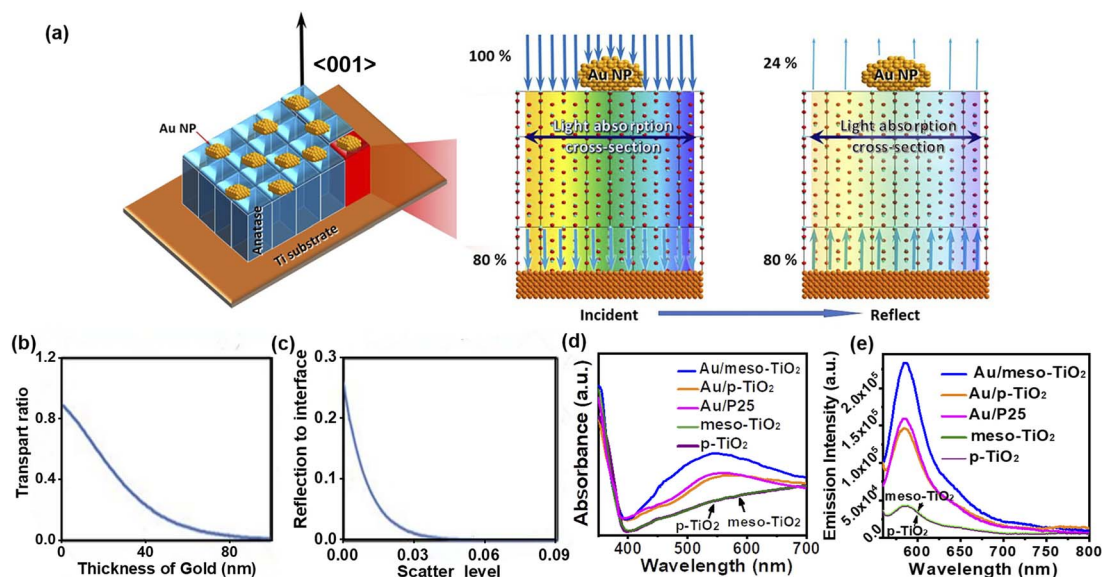

Fig. 2 Optical properties of the as-synthesized samples and the back-reflection models. (a) Scheme demonstrating how additional light interacts with the gold nanoparticles through back reflection from the TiO$_2$-titanium foil. (b) Transmission of light into the TiO$_2$-titanium foil as a function of gold thickness, and (c) reflectivity of light as a function of scattered level. (d) UV-vis absorption spectra. (e) Fluorescence spectra; rhodamine B (RhB) was used as the target fluorophore.

4754 | *J. Mater. Chem. A*, 2023, **11**, 4751–4757

This journal is © The Royal Society of Chemistry 2023

Au/*meso*-TiO$_2$, Au/*p*-TiO$_2$ and Au/P25 samples, which are not close-packed, calculations reveal that a minimum of 82% of visible light incident on the Au NP layer can be transmitted into the substrate (Fig. 2b and c). Due to the uniformity of the oriented *meso*-TiO$_2$ film consisting of vertically aligned anatase crystals, Au/*meso*-TiO$_2$ can be assumed to exhibit negligible light scatter at visible wavelengths. Hence, it can be expected to permit light reflected off the substrate back to the Au NPs on the top surface. The overall light harvested by the Au NPs is thus increased, as well as the intensity of the fringing EM field around the Au NPs.[26–29] In comparison, the *p*-TiO$_2$ and P25 film samples with a disordered polycrystalline structure have a much higher light scatter than the oriented *meso*-TiO$_2$ film. Therefore, they cannot reflect light efficiently, thus making it difficult to enhance light harvesting of Au NPs as a consequence. A similar back reflection mechanism has also been shown to be responsible for enhancing surface-enhanced Raman scattering in a sapphire substrate coated with a thin gold film.[14]

The light-harvesting behavior of each sample was measured by UV-vis adsorption spectra and fluorescence spectroscopy. The Au/TiO$_2$ samples all exhibited intense light absorption in the visible light region with the absorption peak centered at 540 nm corresponding to the intrinsic localized surface plasmon resonance peak. It should be noted that the visible-light harvesting capability of the Au/*meso*-TiO$_2$ sample is 1.7 times higher than that of the Au/*p*-TiO$_2$ sample and 1.6 times higher than that of the Au/P25 sample (Fig. 2d), indicating significantly enhanced light harvesting by the Au/*meso*-TiO$_2$ sample. The weak visible light absorption of the TiO$_2$ samples is partially due to the defects that widen the adsorption to visible light, as reported in our previous work,[25] and partially due to the light absorbance of Ti foil (Fig. S8a†). Furthermore, the clearly enhanced fluorescence emission from the RhB on the Au/TiO$_2$ samples excited by the strong LSPR of Au NPs was also demonstrated (Fig. 2e). The strongest fluorescence emission of Au/*meso*-TiO$_2$ indicates that the excitation and, thus the electromagnetic field (EM) intensity in that sample is the most intense.[30] Moreover, the band potentials of *meso*-TiO$_2$ and *p*-TiO$_2$ were measured by Mott–Schottky measurement to compare their energy positions. As shown in Fig. S8b and c,† the same flat-band potential (equal to the CB in n-type semiconductor) for *meso*-TiO$_2$ and *p*-TiO$_2$ were measured at −0.32 eV *vs.* Ag/AgCl, while a similar, optical band gap was confirmed from the UV-vis spectra, indicating that the conduction and valence band edge positions of *meso*-TiO$_2$ and *p*-TiO$_2$ are similar. It is therefore safe to assume that the enhanced visible light harvesting capability and intense EM field of Au/*meso*-TiO$_2$ compared to those of Au/*p*-TiO$_2$ is attributed to the TiO$_2$-effect induced efficient utilization of reflected light.

3.2 Photocatalytic activity evaluation

Given that Au/*meso*-TiO$_2$ displays the greatest visible light absorption and intense fringing EM field, it might be expected to exhibit superior photocatalytic performance to the other two samples. The visible light photocatalytic performance of the catalysts was evaluated for two model reactions: CH$_3$SH removal

and hydrogen production from water. The samples immobilized on Ti foil were cut into 1 × 1 cm^2 plates, and the light was vertically incident onto the sample (Fig. S9†). As shown in Fig. 3a, *meso*-TiO$_2$, *p*-TiO$_2$, and P25 appeared to have no activity when exposed to visible light, while Au/*meso*-TiO$_2$ exhibited significant photocatalytic activity toward aerobic CH$_3$SH decomposition. An enhanced CH$_3$SH decomposition (92.2%) was demonstrated by Au/*meso*-TiO$_2$ under visible light irradiation, compared to 51.0% for Au/*p*-TiO$_2$ (51.0%) and 69.9% for Au/P25. The higher catalytic efficiency of Au/P25 than that of Au/*p*-TiO$_2$ could be attributed to the mix-phased P25 with high charge carrier transportation and separation properties. Meanwhile, the results of CH$_3$SH adsorption (Fig. S10†) confirm that CH$_3$SH prefers to be adsorbed on Au NPs.

Photocatalytic H$_2$ evolution was conducted by inserting the samples at the bottom of a cylindrical quartz cell filled with a water/methanol mixture. It is worth noting that the H$_2$ production of Au/*meso*-TiO$_2$ (518.46 µL cm^{-2}) is 1.8-fold greater than that of Au/*p*-TiO$_2$ (287.99 µL cm^{-2}), and 1.4-fold higher than that displayed by Au/P25 (375.40 µL cm^{-2}) (Fig. 3b), while only small amounts of H$_2$ were evolved from *meso*-TiO$_2$ (30.86 µL cm^{-2}), *p*-TiO$_2$ (25.12 µL cm^{-2}) and P25 (29.60 µL cm^{-2}) due to their inactivity under visible light. Furthermore, the results of the cyclic experiments with Au/*meso*-TiO$_2$ demonstrate its good stability toward photocatalytic CH$_3$SH removal and H$_2$ evolution (Fig. S11†). As shown above, the efficiency of both CH$_3$SH removal and H$_2$ production catalyzed by the Au/*meso*-TiO$_2$ sample is higher than those displayed by Au/*p*-TiO$_2$ or Au/P25 samples. Given the considerable difference in catalytic performance but the almost identical content, size and morphology of Au NPs in these samples, the superior photocatalytic performance of Au/*meso*-TiO$_2$ can be attributed to support-effect induced efficient utilization of reflected light.

3.3 Mechanistic insights into enhanced photocatalytic activity

The results of reaction suppression by the chemical scavengers reveal that light-generated electron (e$^-$), hole (h$^+$), ·O$_2$$^-$, and
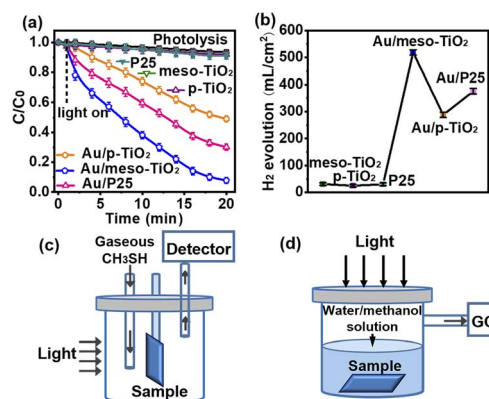

Fig. 3 The photocatalytic performance of the as-synthesized samples under visible light irradiation. (a) The elimination efficiency of odorous CH$_3$SH. (b) H$_2$ evolution. Schematic diagrams of the equipment for (c) CH$_3$SH oxidation and (d) water splitting, respectively.

This journal is © The Royal Society of Chemistry 2023

J. Mater. Chem. A, 2023, **11**, 4751–4757 | **4755**

˙OH are the main reactive species for photocatalytic redox reactions (Fig. S12b†).[34–36] In the photocatalytic oxidation of CH_3SH, the reactive oxygen species (ROSs) oxidize CH_3SH into SO_4^{2-} (see the IC results in Table S2†). During photocatalytic H_2 evolution, the electrons transferred from Au NPs to TiO_2 reduce H_2O to H_2, while the oxidative ROSs react with methanol (sacrificial agent) in the water/methanol mixed solution.[34] As shown in Fig. 4a and S12a,† the photocurrent of Au/*meso*-TiO_2 is 1.9 times and 1.5 times higher than that of Au/*p*-TiO_2 and Au/P25, respectively. The photocurrent is derived from the LSPR-induced electron transfer from plasmonic Au NPs to the conduction band of TiO_2.[31–33]

The increased photocurrent of Au/*meso*-TiO_2 reveals that the better light harvesting capability of Au/*meso*-TiO_2 could influence the photocurrent. To identify the generation of ROSs in the samples, we conducted an electron spin resonance (ESR) study. The ESR spectra in Fig. 4b and c show a stronger signal of ˙OH and ˙O_2^- radicals in the Au/*meso*-TiO_2 sample than that observed with the Au/TiO_2-60 sample under identical visible light irradiation, confirming that Au/*meso*-TiO_2 was better able to generate ROSs. As more photoexcited electrons and ROSs are generated by the Au/*meso*-TiO_2 catalyst, deep oxidation of CH_3SH and improved photocatalytic H_2 evolution were achieved with this photocatalyst. Fig. 4d illustrates the photocatalytic performance of Au/*meso*-TiO_2 for the oxidation of CH_3SH at different incident light intensities. When the light intensity is raised, the CH_3SH removal rate increases. Clearly, the stronger the light absorption, the higher the reaction performance. We have shown experimentally and through simulations that the utilization of reflected light can enhance the light-harvesting ability of Au NPs for efficient photocatalytic reaction. This light reflection-enhanced architecture with conductive Ti foil as a substrate also has potential for application in other fields of solar energy conversion, such as photoelectrochemistry and solar cells.[37–39]

4. Conclusions

In summary, this study reported a novel strategy to enhance the visible light-harvesting capability of Au NPs by depositing Au NPs on a film of vertically <001> oriented anatase mesocrystals adhered on a piece of Ti foil for improved photocatalytic performance in both S-VOC elimination and H_2 evolution. This architecture enhances the visible light harvesting of Au NPs by increasing the absorption of the back-reflection of transmitted light. The enhanced light absorption increases the intensity of the fringing electromagnetic field near the Au NPs, improving the catalytic activity. Our work demonstrates that light-harvesting of plasmonic catalysts can be enhanced through a light reflection-promoted optical absorption model. This research could inspire a new paradigm to construct efficient visible light photocatalysts that are also expected to be applied to photoelectrochemistry and solar cells.

Author contributions

Experiments, J. Y. and S. H.; conceptualization, H. Y. Z. and M. W.; TEM analysis, H. L.; reflection analysis, E. J. and E. R. W,; simulation, J. Q.; result analysis S. S, C. H. and S. H.; investigation, X. Y. W. and Y. C. J.; mechanism, H. Y. Z., H. L., S. S. and E. R. W.; writing, J. Y., M. W., E. R. W. and H. Y. Z.; funding acquisition, M. W. and E. R. W. All authors contributed to revision and approved the final version of the manuscript.

Conflicts of interest

The authors declare no competing financial interest.

Acknowledgements

Fig. 4 (a) Photocurrent responses of samples under visible-light irradiation (λ > 430 nm). DMPO spin-trapping ESR spectra (b) for DMPO − ˙OH and (c) for DMPO − ˙O_2^- irradiated under visible light. (d) Dependence of the catalytic activity of CH_3SH removal by Au/*meso*-TiO_2 on the irradiation intensity.

References

1 A. Holm, E. D. Goodman, J. H. Stenlid, A. Aitbekova, R. Zelaya, B. T. Diroll, A. C. Johnston-Peck, K.-C. Kao, C. W. Frank, L. G. M. Pettersson and M. Cargnello, *J. Am. Chem. Soc.*, 2020, **142**, 14481–14494.

2 Y. Gao, W. Nie, Q. Zhu, X. Wang, S. Wang, F. Fan and C. Li, *Angew. Chem., Int. Ed.*, 2020, **59**, 18218.

3 D. Tsukamoto, Y. Shiraishi, Y. Sugano, S. Ichikawa, S. Tanaka and T. Hirai, *J. Am. Chem. Soc.*, 2012, **134**, 6309–6315.
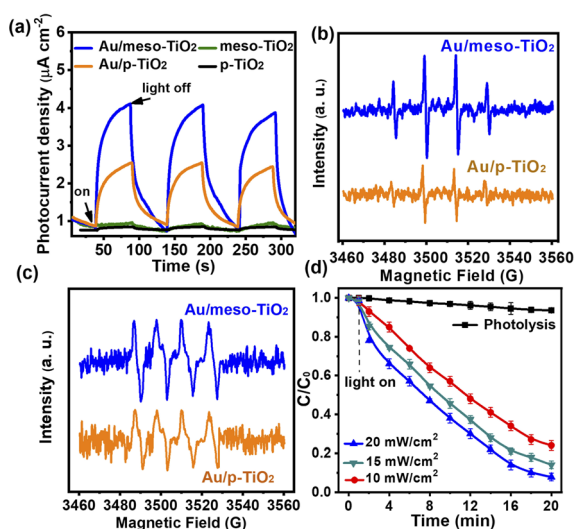
4 A. Grirrane, A. Corma and H. García, *Science*, 2008, **322**, 1661–1664.

5 A. Primo, A. Corma and H. García, *Phys. Chem. Chem. Phys.*, 2011, **13**, 886–910.

6 S.-i. Naya and H. Tada, *J. Catal.*, 2018, **364**, 328–333.

7 S. Wang, Y. Gao, S. Miao, T. Liu, L. Mu, R. Li, F. Fan and C. Li, *J. Am. Chem. Soc.*, 2017, **139**, 11771–11778.

8 H. Li, S. Wang, M. Wang, Y. Gao, J. Tang, S. Zhao, H. Chi, P. Zhang, J. Qu, F. Fan and C. Li, *Angew. Chem.*, 2022, **134**, e202204272.

9 Y. Tian and T. Tatsuma, *J. Am. Chem. Soc.*, 2005, **127**, 7632–7637.

10 S. K. Cushing, J. Li, J. Bright, B. T. Yost, P. Zheng, A. D. Bristow and N. Wu, *J. Phys. Chem. C*, 2015, **119**, 16239–16244.

11 M. J. Kale, T. Avanesian and P. Christopher, *ACS Catal.*, 2014, **4**, 116–128.

12 J. Li, S. K. Cushing, F. Meng, T. R. Senty, A. D. Bristow and N. Wu, *Nat. Photon.*, 2015, **9**, 601–607.

13 E. Peiris, S. Sarina, E. R. Waclawik, G. A. Ayoko, P. Han, J. Jia and H. Y. Zhu, *Angew. Chem., Int. Ed.*, 2019, **58**, 12032–12036.

14 M. W. Knight, Y. Wu, J. B. Lassiter, P. Nordlander and N. J. Halas, *Nano Lett.*, 2009, **9**, 2188–2192.

15 J. Zhang, X. Jin, P. I. Morales-Guzman, X. Yu, H. Liu, H. Zhang, L. Razzari and J. P. Claverie, *ACS Nano*, 2016, **10**, 4496–4503.

16 Y. Kim, J. G. Smith and P. K. Jain, *Nat. Chem.*, 2018, **10**, 763–769.

17 P. Christopher and M. Moskovits, *Annu. Rev. Phys. Chem.*, 2017, **68**, 379–398.

18 U. Aslam, V. G. Rao, S. Chavez and S. Linic, *Nat. Catal.*, 2018, **1**, 656–665.

19 C.-Y. Li, S. Duan, B.-Y. Wen, S.-B. Li, M. Kathiresan, L.-Q. Xie, S. Chen, J. R. Anema, B.-W. Mao, Y. Luo, Z.-Q. Tian and J.-F. Li, *Nat. Nanotechnol.*, 2020, **15**, 922–926.

20 Q. Tang, J. Wu, D. Kim, C. Franco, A. Terzopoulou, A. Veciana, J. Puigmartí-Luis, X. Z. Chen, B. J. Nelson and S. Pané, *Adv. Funct. Mater.*, 2022, **32**, 2202180.

21 D. Xia, W. Xu, Y. Wang, J. Yang, Y. Huang, L. Hu, C. He, D. Shu, D. Y. C. Leung and Z. Pang, *Environ. Sci. Technol.*, 2018, **52**, 13399–13409.

22 J. Yang, Q. Zhang, F. Zhang, D. Xia, H. Liu, S. Tian, L. Sun, D. Shu, C. He and S. Runa, *J. Hazard. Mater.*, 2018, **358**, 136–144.

23 E. Jin, Z. Lan, Q. Jiang, K. Geng, G. Li, X. Wang and D. Jiang, *Chem*, 2019, **5**, 1632–1647.

24 Y.-H. Lai, S.-W. Chen, M. Hayashi, Y.-J. Shiu, C.-C. Huang, W.-T. Chuang, C.-J. Su, H.-C. Jeng, J.-W. Chang, Y.-C. Lee, A.-C. Su, C.-Y. Mou and U. S. Jeng, *Adv. Funct. Mater.*, 2014, **24**, 2544–2552.

25 J. Yang, Q. Wu, S. He, J. Yan, J. Shi, J. Chen, M. Wu and X. Yang, *Nanoscale*, 2015, **7**, 13888–13897.

26 Z. Qiu, K. S. Wong, M. Wu, W. Lin and H. Xu, *Appl. Phys. Lett.*, 2004, **84**, 2739–2741.

27 T. W. van Deelen, C. Hernández Mejía and K. P. de Jong, *Nat. Catal.*, 2019, **2**, 955–970.

28 X. Liu, Y. Shi, Y. Jin, T. Tana, E. Peiris, X. Zhang, F. Xu, E. R. Waclawik, S. E. Bottle, H. Zhu and S. Sarina, *Angew. Chem.*, 2022, **134**, e202203158.

29 S. Atta, A. M. Pennington, F. E. Celik and L. Fabris, *Chem*, 2018, **4**, 2140–2153.

30 S. Lee, B. A. Apgar and L. W. Martin, *Adv. Energy Mater.*, 2013, **3**, 1084–1090.

31 X.-S. Li, X.-Y. Ma, J.-L. Liu, Z.-G. Sun, B. Zhu and A.-M. Zhu, *Catal. Today*, 2019, **337**, 132–138.

32 E. Kazuma, J. Jung, H. Ueba, M. Trenary and Y. Kim, *Science*, 2018, **360**, 521–526.

33 Y. Negrín-Montecelo, M. Testa-Anta, L. Marín-Caba, M. Pérez-Lorenzo, V. Salgueiriño, M. A. Correa-Duarte and M. Comesaña-Hermo, *Nanomaterials*, 2019, **9**, 990.

34 N. L. Reddy, V. N. Rao, M. Vijayakumar, R. Santhosh, S. Anandan, M. Karthik, M. V. Shankar, K. R. Reddy, N. P. Shetti, M. N. Nadagouda and T. M. Aminabhavi, *Energy*, 2019, **44**, 10453–10472.

35 K. Yang, J. Liu, R. Si, X. Chen, W. Dai and X. Fu, *J. Catal.*, 2014, **317**, 229–239.

36 J. Yang and C.-Y. Mou, *Appl. Catal., B*, 2018, **231**, 283–291.

37 Y. Wang, J. Zhang, W. Liang, H. Yang, T. Guan, B. Zhao, Y. Sun, L. Chi and L. Jiang, *CCS Chem.*, 2022, **4**, 1153–1168.

38 P. S. Tóth, G. Szabó, G. Bencsik, G. F. Samu, K. Rajeshwar and C. Janáky, *SusMat*, 2022, **2**, 749–760.

39 R. Shi, L. Shang, C. Zhou, Y. Zhao and T. Zhang, *Exploration*, 2022, **2**, 20210046.

This journal is © The Royal Society of Chemistry 2023

J. Mater. Chem. A, 2023, **11**, 4751–4757 | **4757**